

University of Groningen

Quantifying suppression of the cosmological 21-cm signal due to direction dependent gain calibration in radio interferometers

Mouri Sardarabadi, A.; Koopmans, L.V.E.

Published in:
Monthly Notices of the Royal Astronomical Society

DOI:
[10.1093/mnras/sty3444](https://doi.org/10.1093/mnras/sty3444)

IMPORTANT NOTE: You are advised to consult the publisher's version (publisher's PDF) if you wish to cite from it. Please check the document version below.

Document Version
Publisher's PDF, also known as Version of record

Publication date:
2019

[Link to publication in University of Groningen/UMCG research database](#)

Citation for published version (APA):

Mouri Sardarabadi, A., & Koopmans, L. V. E. (2019). Quantifying suppression of the cosmological 21-cm signal due to direction dependent gain calibration in radio interferometers. *Monthly Notices of the Royal Astronomical Society*, 483(4), 5480–5490. <https://doi.org/10.1093/mnras/sty3444>

Copyright

Other than for strictly personal use, it is not permitted to download or to forward/distribute the text or part of it without the consent of the author(s) and/or copyright holder(s), unless the work is under an open content license (like Creative Commons).

Take-down policy

If you believe that this document breaches copyright please contact us providing details, and we will remove access to the work immediately and investigate your claim.

Downloaded from the University of Groningen/UMCG research database (Pure): <http://www.rug.nl/research/portal>. For technical reasons the number of authors shown on this cover page is limited to 10 maximum.

Quantifying suppression of the cosmological 21-cm signal due to direction-dependent gain calibration in radio interferometers

A. Mouri Sardarabadi[★] and L. V. E. Koopmans[★]

Kapteyn Astronomical Institute, University of Groningen, PO Box 800, NL-9700 AV Groningen, the Netherlands

Accepted 2018 December 15. Received 2018 December 15; in original form 2018 September 10

ABSTRACT

The 21-cm signal of neutral hydrogen promises to be an important source of information for the study of the cosmic dawn and epoch of reionization. However, its detection is difficult without sufficient mitigation of strong contaminating signals in the data, requiring accurate instrument gain calibration. To detect the 21-cm signal, one analyses the resulting post-calibration residual data. The 21-cm signal residing in these residuals, however, can be strongly affected by the process of direction-dependent calibration (DDC) combined with sky-model removal. The impact of this, in particular on the frequency behaviour of the 21-cm signal, has remained poorly quantified. In this paper, we derive a new mathematical formalism on how to calculate the suppression of the 21-cm signal during DDC and sky-model removal. We also show how a priori information about the frequency behaviour of the instrument, such as spectral smoothness, can be utilized to reduce signal suppression. The theoretical results are tested using a realistic simulation based on the LOFAR-EoR calibration set-up. The results show that if the instrumental gains are intrinsically smooth over several MHz (e.g. polynomials over a bandwidth of ~ 10 MHz), this is sufficient to allow for DDC in as many as ~ 100 directions with limited and quantifiable suppression of the 21-cm signal power spectrum. We also demonstrate that more incomplete sky models during calibration lead to larger 21-cm signal suppression, even if the instrumental gain models are fully smooth. This result has immediate consequences for future radio telescopes with non-identical station beams, where DDC might be necessary (e.g. SKA-Low).

Key words: instrumentation: interferometers – methods: analytical – dark ages, reionization, first stars.

1 INTRODUCTION

Studying the redshifted 21-cm hyperfine transition line of neutral hydrogen (called the ‘21-cm signal’ hereafter) originated from the infant Universe is one of the most powerful methods for gaining insight into the evolution of our Universe (see e.g. Furlanetto, Peng Oh & Briggs 2006b; Morales & Wyithe 2010; Pritchard & Loeb 2012, for reviews). The signals generated at a radio receiver in response to these radiations are extremely weak, and their detection is a challenging task which requires highly sensitive instruments (e.g. Furlanetto, Oh & Briggs 2006a; McQuinn et al. 2006; Harker et al. 2010; Parsons et al. 2012; Beardsley et al. 2013; Koopmans et al. 2015; DeBoer et al. 2017). Modern radio telescopes, such as the LOFAR Frequency Array (LOFAR) in the Netherlands, extend over large distances and combine many receivers to boost both their sensitivity (i.e. collecting area) and angular resolution (see van Haarlem et al. 2013, for details). However, the signal of interest is not the

only source of radiation. There are many natural radiators, such as our own Milky Way and other (radio) galaxies, which also generate detectable signals at the receivers, often exceeding the 21-cm signal by many orders of magnitude. Separating these different (partly polarized) signals is an essential part of the detection process (e.g. Di Matteo et al. 2002; Oh & Mack 2003; Jelić et al. 2008; Asad et al. 2015; Mertens, Ghosh & Koopmans 2018). During the observation with a radio telescope, knowledge of the known radio sources, a.k.a. the ‘sky model’, is often used to estimate the unknown (time and frequency dependent) parameters of the telescope which can affect the measurements. This process is called ‘calibration’ and will be discussed in more details in Section 3. Calibration is an integral part of the data processing of a radio telescope and has been extensively studied in the context of aperture arrays such as LOFAR (e.g. Boonstra & van der Veen 2003; Wijnholds & van der Veen 2009; Kazemi, Yatawatta & Zaroubi 2013; Mouri Sardarabadi & van der Veen 2014; Smirnov & Tasse 2015; Yatawatta 2015). As the resolution and sensitivity of the instruments increase, more foreground sources can be detected, and often many of the fainter or more diffuse sources which are not included in the sky model during the

[★] E-mail: ammsa@astro.rug.nl (AMS); koopmans@astro.rug.nl (LVEK)

calibration process. This exclusion of actual sources leads to ‘sky- or model-incompleteness’ and can result in several artefacts in the final data (e.g. Grobler et al. 2014, 2016; Barry et al. 2016; Patil et al. 2016; Wijnholds, Grobler & Smirnov 2016; Ewall-Wice et al. 2017). It is therefore vital to make a distinction between the known and unknown foreground sources. The 21-cm signal and often also the extended diffuse Galactic foreground (even if known) are not part of the sky model either because they are often too faint or too complicated to be described by a limited set of model parameters. In our analysis, we are interested in (possible) corruptions of the desired signal, i.e. the weak 21-cm signal in our case, as a result of the process of calibration. We also study the effect of sky-model incompleteness and the frequency behaviour of the instrument. However, the mathematical framework introduced in this analysis is not limited to 21-cm signal studies and can easily be extended to any signal of interest. Our approach also extends previous analyses to that of direction-dependent calibration (DDC), which is likely necessary for instruments for non-identical receiver beams. In Section 2, we discuss the commonly used signal processing data model or measurement equation and our assumptions. Based on this model we formulate calibration as a least squares optimization problem in Section 3 and then proceed to study the effects of such calibration on the desired signals. In Section 4, we use parameters from the LOFAR telescope to study the effect of calibration by comparing the spectra before and after calibration. In Section 5, we draw our conclusions.

2 THE RADIO TELESCOPE DATA MODEL

Below we describe our assumptions first, followed by the mathematical data model. The following table summarizes the important quantities used in this and following sections:

| | |
|--------------------|--|
| P | number of receivers (e.g. stations or dishes) |
| Q | number of clusters |
| K | number of frequency channels |
| T | number of snapshots used for single calibration run |
| N | is the number of samples used to generate a single visibility sample |
| $\hat{\mathbf{R}}$ | is a $P \times P$ Hermitian matrix where its element $[\hat{\mathbf{R}}]_{i,j}$ is the visibility for receivers i and j |
| \mathbf{R} | is the model/measurement equation for $\hat{\mathbf{R}}$ in the matrix form |
| $\hat{\mathbf{f}}$ | is the flagged data vector of length $TKP^2 \times 1$ |
| \mathbf{r} | is the flagged model/measurement equation for $\hat{\mathbf{f}}$ |
| $\mathbf{g}_{q,k}$ | is a $P \times 1$ vector representing the complex gains of the receivers for cluster q at channel k , with $q = 1, \dots, Q$ and $k = 1, \dots, K$. |

2.1 Assumptions in the data model

In this analysis, we assume to have access to the sampled output of P receivers (together called an ‘array’) which are exposed to electromagnetic radiation from extraterrestrial radio sources. It is possible for each receiver to be a beam-formed array itself, and the model presented here is adequate for any general array topology (see for example the hierarchical structure of the LOFAR telescope; van Haarlem et al. 2013). As a result of Earth rotation, the apparent position of the sources changes in time, as does the array for a reference point on the sky. We assume that the sources are stationary (i.e. do not change in brightness or structure) during the observation

of N samples of the electromagnetic signal/voltages in time. A single observation with N samples is denoted as a ‘snapshot’ in time. We also assume that the output is divided into K frequency channels for which the narrow-band assumption hold (e.g. Wijnholds & van der Veen 2009; Mouri Sardarabadi 2016). We used the same sky model given by Yatawatta (2015) in our numerical simulations, where the sources in the sky are grouped spatially into so-called ‘clusters’. During the calibration process, we assume that all sources within a cluster are affected by the same complex and direction-dependent gain.¹ In this work, we assume that the sky is unpolarized. The gains can change both in amplitude and phase for example due to instrumental and also ionospheric effects.

2.2 Mathematical framework

For a single snapshot and frequency channel, we can write the model for the voltage output of the array as

$$\mathbf{y}[n] = \sum_q \mathbf{G}_q \mathbf{s}_q[n] + \mathbf{n}[n], \quad (1)$$

where $n = 1, \dots, N$ is the sample index, $\mathbf{y}[n]$ is a $P \times 1$ vector obtained by stacking the output of each receiver, $q = 1, \dots, Q$ is the cluster index, $\mathbf{G}_q = \text{diag}(\mathbf{g}_q)$ is a $P \times P$ diagonal matrix with \mathbf{g}_q as its diagonal representing the gains (of all receivers) for the q th cluster, $\mathbf{s}_q[n]$ is a $P \times 1$ vector representing the sampled signal from sources in q th cluster, and $\mathbf{n}[n]$ is the total receiver noise contribution to the output, coming from the system and its electronics. We assume that the system noise and the signals from each direction are independent Gaussian random variables with zero mean. The covariance model for a single snapshot and channel follows from this assumption as

$$\mathbf{R} = \mathcal{E}\{\mathbf{y}\mathbf{y}^H\} = \sum_q \mathbf{G}_q \boldsymbol{\Sigma}_q \mathbf{G}_q^H + \mathbf{R}_n, \quad (2)$$

where $\boldsymbol{\Sigma}_q = \mathcal{E}\{\mathbf{s}\mathbf{s}^H\}$ is the covariance of the signal from q th cluster (or ‘direction’) and $\mathbf{R}_n = \mathcal{E}\{\mathbf{n}\mathbf{n}^H\}$ is the noise covariance matrix. An entry of the covariance matrix for two receivers is called a (complex) visibility, and the vector connecting two receivers is called a baseline. There could be many visibility samples for a particular baseline pair as a function of time and frequency. Due to various model imperfections, such as the existence of radio frequency interference near some receivers, it is common to remove some receiver pairs from the data (e.g. Offringa, Van De Gronde & Roerdink 2012; Offringa et al. 2013, 2015; Sokolowski, Wayth & Lewis 2016). We denote by \mathbf{M} the symmetric masking matrix which consists of zeros and ones and is used to indicate which pairs are removed. We also remove entries where \mathbf{R}_n is dominant, which for uncorrelated noise are the diagonal elements, called the autocorrelation (or the zero-baseline/spacing visibilities). A noisy estimate of the reduced covariance matrix can be directly obtained from the $P \times N$ data matrix collected during a single snapshot observation. This estimate is called a sample covariance matrix and defined as

$$\hat{\mathbf{R}} = \mathbf{M} \odot \frac{1}{N} \sum_{n=1}^N \mathbf{y}[n]\mathbf{y}[n]^H, \quad (3)$$

¹In reality the gains also vary spatially inside a cluster, but given that the simulation of the visibilities involves station-beam formation, this automatically generates direction-dependent gain effects in the data inside clusters. The first-order recovery of the 21-cm signal, as shown later, shows that the assumption of a constant gain inside a cluster during modelling is therefore still of second order.

where \odot is the Hadamard or element-wise product. Let $k = 1, \dots, K$ be the index for each measured frequency channel and $t = 1, \dots, T$ be the index for each time snapshot, then we denote the measured sampled covariance matrix (i.e. the visibility data) as $\hat{\mathbf{R}}_{t,k}$ and the corresponding model as $\mathbf{R}_{t,k}$. We assume that the gains remain constant during several snapshots based on the instrument and cluster. In this paper, we take this time to be equal among all clusters and exactly T snapshots, although this is not necessary. The gains can also be assumed constant for several adjacent frequency channels, however this is not used in this analysis and the frequency behaviour of the gains is treated as a continuous and ‘smooth’ function which we will discuss in the following sections in more details. The final model for a single channel and frequency is given by

$$\mathbf{R}_{t,k} = \mathbf{M}_{t,k} \odot \sum_q \mathbf{G}_{q,k} \boldsymbol{\Sigma}_{q,t,k} \mathbf{G}_{q,k}^H, \quad (4)$$

for $k = 1, \dots, K, t = 1, \dots, T$. Note that \mathbf{R}_n causes a bias on the visibilities in the model and it is also a large contributor to the noise on all sampled visibilities. The contribution of \mathbf{R}_n as a bias is removed by \mathbf{M} . During the remainder of this analysis, we use the vectorized form of these matrices, which are defined as

$$\mathbf{r} = \begin{bmatrix} \text{vect}(\mathbf{R}_{1,1}) \\ \text{vect}(\mathbf{R}_{2,1}) \\ \vdots \\ \text{vect}(\mathbf{R}_{T,K}) \end{bmatrix}, \quad \hat{\mathbf{r}} = \begin{bmatrix} \text{vect}(\hat{\mathbf{R}}_{1,1}) \\ \text{vect}(\hat{\mathbf{R}}_{2,1}) \\ \vdots \\ \text{vect}(\hat{\mathbf{R}}_{T,K}) \end{bmatrix}.$$

Based on the model in equation (4), we can now formulate the calibration problem in the next section.

3 DIRECTION-DEPENDENT GAIN CALIBRATION

In this section, we introduce the complex gain model for DDC, starting with the un-regularized least-squares penalty function that is being optimized to obtain the gain solution. We then introduce how the data-model solution can be rewritten into a ‘semilinear’ form and how gain regularization can be included in the solutions. We end this section by describing a data model where part of the visibility data is not used in the calibration step. The scenarios described in Sections 3.1–3.4 cover a large set of calibration methods which are commonly used. They show how to quantify weak signal suppression for both regularized and unregularized problems at convergence (i.e. on a stationary point of the cost function), and how to find an accurate approximation of the signal suppression if an unregularized problem is terminated early.

3.1 Least-squares penalty function

Calibration is the process of estimating the complex gains $\mathbf{g}_{q,k} = \text{vectdiag}(\mathbf{G}_{q,k})$ based on the measured data $\hat{\mathbf{R}}_{t,k}$ and the known sky model $\boldsymbol{\Sigma}_{q,t,k}$. As stated, the sky model can be incomplete. The calibration procedure we address here is a least squares optimization problem of the form

$$\hat{\boldsymbol{\theta}} = \arg \min_{\boldsymbol{\theta}} f(\boldsymbol{\theta}), \quad (5)$$

where $f(\boldsymbol{\theta}) = \frac{1}{2} \|\hat{\mathbf{r}} - \mathbf{r}(\boldsymbol{\theta})\|_2^2$ and

$$\boldsymbol{\theta} = [\mathbf{g}_{1,1}^T, \mathbf{g}_{1,1}^H, \mathbf{g}_{2,1}^T, \mathbf{g}_{2,1}^H, \dots, \mathbf{g}_{Q,K}^T, \mathbf{g}_{Q,K}^H]^T \quad (6)$$

is an augmented vector collating all the unknown parameters. An augmented vector is a vector where a complex variable and its

conjugate are stacked together as two independent variables, and it is used extensively in signal processing literature (see e.g. Schreier 2010, and references therein). We can also formulate this problem as a weighted least square optimization similar to Wijnholds & van der Veen (2009) and Mouri Sardarabadi & van der Veen (2014). For this analysis, we assume the noise behaviour of the visibility samples to be identical, which makes such a weighted formulation unnecessary. Adapting the results to a weighted least squares analysis is trivial. The problem at hand is non-linear and non-convex and several iterative approaches have been proposed to solve it (e.g. Boonstra & van der Veen 2003; Wijnholds & van der Veen 2009; Kazemi et al. 2013; Mouri Sardarabadi & van der Veen 2014; Smirnov & Tasse 2015). In this paper, we do not focus on solving the gains, but discuss possible physical constraints on the properties of the solution, $\hat{\boldsymbol{\theta}}$, once gain solutions are obtained. However, gains are not the only product of the calibration problem. The final residual

$$\mathbf{e} \equiv \hat{\mathbf{r}} - \mathbf{r}(\hat{\boldsymbol{\theta}}) \quad (7)$$

is the target of interest for much scientific research such as the study of extremely faint cosmological 21-cm signals. It is therefore crucial to have a good understanding of the properties of \mathbf{e} . In this analysis, we are interested in possible bias in the form of suppression and the associated baseline-delay (power) spectrum.

3.2 Residuals after least-squares gain calibration

By taking a closer look at the model, we can show (see Appendix A) that for all $\boldsymbol{\theta}$ defined by equation (6), the model, $\mathbf{r}(\boldsymbol{\theta})$, satisfies the following property

$$\mathbf{r}(\boldsymbol{\theta}) = \frac{1}{2} \mathbf{J}(\boldsymbol{\theta}) \boldsymbol{\theta}, \quad (8)$$

where $\mathbf{J}(\boldsymbol{\theta})$ is the Jacobian matrix, defined by

$$\mathbf{J}(\boldsymbol{\theta}) = \frac{\partial \mathbf{r}(\boldsymbol{\theta})}{\partial \boldsymbol{\theta}^T}.$$

We call this property ‘semilinearity’ because it leads to results that appear very similar to the linear least squares problems, as we show in this section. The Jacobian itself is linear in $\boldsymbol{\theta}$ and $\mathbf{J}(\boldsymbol{\theta}_1)\boldsymbol{\theta}_2 = \mathbf{J}(\boldsymbol{\theta}_2)\boldsymbol{\theta}_1$. At a solution, $\hat{\boldsymbol{\theta}}$, the gradient of the cost function must vanish, leading to

$$\left. \frac{\partial f(\boldsymbol{\theta})}{\partial \boldsymbol{\theta}} \right|_{\boldsymbol{\theta}=\hat{\boldsymbol{\theta}}} = \mathbf{J}(\hat{\boldsymbol{\theta}})^H \mathbf{e}(\hat{\boldsymbol{\theta}}) = \mathbf{0}. \quad (9)$$

Using the property above we obtain

$$\mathbf{J}(\hat{\boldsymbol{\theta}})^H \mathbf{J}(\hat{\boldsymbol{\theta}}) \hat{\boldsymbol{\theta}} = 2\mathbf{J}(\hat{\boldsymbol{\theta}})^H \hat{\mathbf{r}},$$

which except for the factor two on the right-hand side, is a standard normal equation. Inserting this result back into the residual in equation (7), we obtain

$$\mathbf{e}(\hat{\boldsymbol{\theta}}) = [\mathbf{I} - \mathbf{J}(\hat{\boldsymbol{\theta}})\mathbf{J}(\hat{\boldsymbol{\theta}})^\dagger] \hat{\mathbf{r}} \equiv \mathbf{P}(\hat{\boldsymbol{\theta}})^\perp \hat{\mathbf{r}}, \quad (10)$$

where (\dagger) is the Moore–Penrose pseudo inverse. For any matrix, \mathbf{A} , the product $\mathbf{P} = \mathbf{A}\mathbf{A}^\dagger$ is an orthogonal projection matrix on to its column space and $\mathbf{P}^\perp \equiv \mathbf{I} - \mathbf{P}$ is the projection matrix for its null space [for more properties of general inverse of matrices see e.g. Rohde (1965)]. For a linear problem this projection matrix is constant while in our semilinear case it is a function of the solutions at stationary points of $f(\boldsymbol{\theta})$. It is important to note that in contrast to linearization techniques, where $\hat{\boldsymbol{\theta}}$ is assumed to be sufficiently close to the (chosen a priori) true solutions, the method presented here assumes closeness to a critical point of the cost function. While the

former is unverifiable, because the true solutions are unknown, the latter can use the norm of the gradient as a verification tool. Hence, the validity of equation (10) can be verified independently of any knowledge about the true solutions. Now we can use equation (10) to study what happens to unmodelled signals in the data. To this end we extend the model for $\hat{\mathbf{r}}$ with several components that are the signal of interest (e.g. the 21-cm signal) plus another unmodelled part of the data (e.g. diffuse foregrounds or unmodelled compact sources). Let the true gain solutions be denoted by $\tilde{\boldsymbol{\theta}}$, then we have

$$\hat{\mathbf{r}} = \mathbf{r}(\tilde{\boldsymbol{\theta}}) + \mathbf{r}_f(\tilde{\boldsymbol{\theta}}) + \mathbf{r}_{21}(\tilde{\boldsymbol{\theta}}) + \boldsymbol{\epsilon},$$

where $\mathbf{r}_f(\tilde{\boldsymbol{\theta}})$ represents any unmodelled foreground signals, $\mathbf{r}_{21}(\tilde{\boldsymbol{\theta}})$ is the unmodelled 21-cm signal, and $\boldsymbol{\epsilon}$ is the finite sample noise on the visibilities. Inserting this model into the expression for the residuals at the solution, we obtain

$$\mathbf{e}(\hat{\boldsymbol{\theta}}) = \mathbf{P}(\hat{\boldsymbol{\theta}})^\perp [\mathbf{r}(\tilde{\boldsymbol{\theta}}) + \mathbf{r}_f(\tilde{\boldsymbol{\theta}}) + \mathbf{r}_{21}(\tilde{\boldsymbol{\theta}}) + \boldsymbol{\epsilon}]. \quad (11)$$

This result can be interpreted as follows:

(1) The first term $\mathbf{P}(\hat{\boldsymbol{\theta}})^\perp \mathbf{r}(\tilde{\boldsymbol{\theta}})$ is the calibration model leakage as the result of the non-linearity of the problem, noise, and model incompleteness. We note that the calibration parameters were estimated using an incomplete model of the sky and are therefore often biased with respect to the truth. This is the main mechanism which causes power of the sky to ‘leak’ into the residuals (e.g. Barry et al. 2016; Ewall-Wice et al. 2017)

(2) The second term $\mathbf{P}(\hat{\boldsymbol{\theta}})^\perp \mathbf{r}_f(\tilde{\boldsymbol{\theta}})$ is the remaining unmodelled foreground signals. There are non-parametric methods that can remove this part in post processing (Mertens et al. 2018). However, the introduced bias on the gain solutions due to this term cannot be corrected for in post processing.

(3) The third term $\mathbf{P}(\hat{\boldsymbol{\theta}})^\perp \mathbf{r}_{21}(\tilde{\boldsymbol{\theta}})$ is what remains of the desired 21-cm signal after the calibration, which makes the suppressed part of the signal exactly $\mathbf{P}(\hat{\boldsymbol{\theta}}) \mathbf{r}_{21}(\tilde{\boldsymbol{\theta}})$.

We want to minimize the first two terms while keeping the third term intact as much as possible. We see that this leads to conflicting objectives. If we model and include sources in \mathbf{r}_f (by adding them to \mathbf{r}), we reduce the model incompleteness and the leakage from the first two terms. However, doing so could increase the degree of freedom in the model which allows for removing even a larger part of the desired signal. In other words, it could increase the rank of the projection matrix, $\mathbf{P}(\hat{\boldsymbol{\theta}})$, and remove more power from \mathbf{r}_{21} . If based on physical arguments, the solution space can be restricted further (e.g. via ‘regularization’), then we can also reduce the signal suppression. There exists a strong physical justification for assuming that the gains are smooth functions of the frequency (van der Tol, Jeffs & van der Veen 2007), which we will discuss next.

3.3 Enforcing smoothness of the gains

In the following, we assume two scenarios. In both cases, we assume that the true gain solutions follow smooth functional forms (e.g. polynomials), where in the first case the higher order (i.e. those describing the gain fluctuations on smaller frequency scale) terms are not regularized but forced on to the lower order function, whereas in the second case they are regularized and allowed to vary around the lower order function.

3.3.1 Gain smoothness via basis-function constraints

We consider enforcing smoothness of the gains utilizing a set of parametric smoothing basis functions. Note that doing so is only

acceptable if the instrument itself shows such behaviour (e.g. an instrument with smooth band-pass). Let the vector $\boldsymbol{\lambda}$ be a $K \times 1$ vector with the central frequency of each channel as its elements. Then we denote by $\Phi(\boldsymbol{\lambda})$ a $K \times M$ unitary basis for the set of sampled smooth functions. For example, for a polynomial of order m , we have $M = m + 1$ and $\Phi(\boldsymbol{\lambda})$ can be obtained from an economical QR or SVD on the following Vandermonde matrix

$$\mathbf{V} = \begin{bmatrix} 1 & \lambda_1 & \lambda_1^2 & \dots & \lambda_1^m \\ & & \vdots & & \\ 1 & \lambda_K & \lambda_K^2 & \dots & \lambda_K^m \end{bmatrix},$$

where we assume $M < K$. One can do this with *any* set of smooth basis functions, e.g. Bernstein polynomials as in Yatawatta (2016). Note that we assume to have access to entire frequency range during a single calibration run, however, if this frequency range is divided into smaller intervals which are calibrated separately, then more generic methods such as splines can be used, which will have a slightly modified Φ (Craven & Wahba 1978). We will drop the dependency on $\boldsymbol{\lambda}$ from the notation as it is assumed not to change during a single calibration run of T snapshots. Using Φ we can model the gains as

$$\boldsymbol{\theta} = (\Phi \otimes \mathbf{I}_{2PQ}) \boldsymbol{\alpha}, \quad (12)$$

where the entries of $\boldsymbol{\alpha}$ are the coefficients for the smooth functions, \mathbf{I}_{2PQ} is an identity matrix of size $2PQ$, and \otimes is the Kronecker product. Note that the only change in the analysis of the previous section is the definition of the Jacobian which then becomes

$$\mathbf{J}_s(\boldsymbol{\alpha}) = \mathbf{J}(\boldsymbol{\theta})(\Phi \otimes \mathbf{I}_{2PQ}).$$

The semilinearity is retained by this change of variable, while the column dimension of \mathbf{J} is reduced by a factor of K/M (e.g. for LOFAR this factor can be more than a hundred for calibration of hundreds of channels with a low-order polynomial). If accurate, this model should reduce the 21-cm signal suppression substantially, while not increasing the leakage from the sky model into the residuals. The foreground leakage (i.e. the unmodelled nuisance part of the data which is not of interest to the analysis of the desired signal) can increase, but as before we assume this to be solved in a post-processing step.

3.3.2 Regularization of high-order gain model terms

Direction-dependent calibration is typically done on time-scales of several minutes (e.g. ~ 10 min for LOFAR) for a data set of hundreds of hours. This means the variation in gains for different clusters, especially the ones further from the centre of the main beam, can be large. Choosing a fixed basis function might not be enough. In this scenario a possible solution is to allow wider set of basis functions, or equivalently enlarge M and allow for more flexibility in Φ , while penalizing the newly added dimensions with a regularization term. We will investigate this here. Let $M = M_1 + M_2$ such that we can split the enlarged Φ as

$$\Phi = [\Phi_1, \Phi_2],$$

where Φ_2 is the extra added freedom. In this case we have $\boldsymbol{\theta} = (\Phi_1 \otimes \mathbf{I}_{2PQ}) \boldsymbol{\alpha}_1 + (\Phi_2 \otimes \mathbf{I}_{2PQ}) \boldsymbol{\alpha}_2$, which is a smooth function with an additional ‘less’ smooth variation around it. By limiting the magnitude of $\boldsymbol{\alpha}_2$, we control this additional term. We can formulate

this approach as a new optimization problem

$$\hat{\theta} = \arg \min_{\theta} f(\theta) + \sum_q \gamma_q \theta_q^H (\Phi_2 \Phi_2^H \otimes \mathbf{I}_{2P}) \theta_q$$

subject to $\mathbf{P}_{\Phi}^{\perp} \theta = \mathbf{0}$,

where $\mathbf{P}_{\Phi} = \Phi \Phi^H \otimes \mathbf{I}_{2PQ}$, γ_q is a regularization parameter, and θ_q is the subset of θ corresponding to q th cluster. This model still enforces a smooth solution of a polynomial of (maximally) order $M - 1$, but if the regularization is large, the solution reduces back to a polynomial of order $M_1 - 1$, as in the case discussed in previous section. Standard regularization (e.g. Tikhonov) around a smooth function would be equivalent to letting $M_2 = K - M_1$, which could be a large number (depending on the number of frequency channels). The regularization parameters can be chosen based on the statistics of the gains, if they are known, or by updating them during optimization. Here we assume that the regularization parameters, while (possibly) different for each cluster, are constant values during a single calibration run of T time samples. The constraint $\mathbf{P}_{\Phi}^{\perp} \theta = \mathbf{0}$ is a different way of stating equation (12) in the optimization setting, forcing the solution to be a low-order polynomial, while $\theta_q^H (\Phi_2 \Phi_2^H \otimes \mathbf{I}_{2P}) \theta_q$ suppresses the contribution of Φ_2 to the solution depending on the level of regularization (i.e. values of γ_q). Using the semilinearity again, we can show (see Appendix B) that in this case the residuals are given by $\mathbf{e}(\hat{\theta}) = [\mathbf{I} - \mathbf{Z}(\hat{\theta})] \hat{\mathbf{r}}$ where

$$\mathbf{Z}(\theta) = \mathbf{J}(\theta) [\mathbf{P}_{\Phi} \mathbf{J}(\theta)^H \mathbf{J}(\theta) \mathbf{P}_{\Phi} + 2\Gamma(\Phi_2 \Phi_2^H \otimes \mathbf{I}_{2PQ})]^{\dagger} \mathbf{J}(\theta)^H,$$

and Γ is a diagonal matrix with QK blocks of the form $\gamma_q \mathbf{I}_{2P}$. Note that, due to regularization, the matrix \mathbf{Z} is not a projection. However, the expression for the residual still allows us to calculate the suppression exactly for a given solution $\hat{\theta}$, the basis functions in Φ and a set of regularization parameters γ_q in a similar way to the previous section. The interpretation of leakage terms remains valid. The exact interpretation of \mathbf{Z} is beyond the scope of this paper, however, in Appendix B we derive the expression for \mathbf{Z} from a Bayesian perspective, which provides some statistical insight for interpreting its effects on the solution.

3.3.3 Effect of early termination on signal suppression

Given the large number of calibration runs that must be performed for long observations, it is essential to know if we can relax the stopping criteria for the applied algorithms. In this section, we motivate how the results we derived for the regularized calibration problem can be used to approximate the effects of the early termination of a constrained problem. Here we assume to have access to an algorithm that solves for a smooth solution using a single basis set equivalent to the scenario in Section 3.3.1 (i.e. $M = M_1$). We also assume that the chosen algorithm does not enforce the constraint $\mathbf{P}_{\Phi}^{\perp} \theta = \mathbf{0}$ at each iteration and it is terminated before full convergence (e.g. an early terminated ADMM algorithm). By translating this constrained problem into a regularized problem, we can approximate its behaviour. We allow Φ_2 to ‘fill’ the entire parameter space or equivalently let $M_2 = K - M_1$. For this regularized problem we have $\mathbf{P}_{\Phi} = \mathbf{I}$ and $\Phi_2 \Phi_2^H = \mathbf{I} - \Phi_1 \Phi_1^H$. The entire regularization is then specified by Φ_1 , which must be the case because the original problem assumes M_2 to be zero. This approach allows for more fluctuations in the solutions, but the amplitude of these fluctuations is limited because of the regularization. Hence, by increasing the regularization parameters, we simulate the effect of increasing the number of iterations. In the limit, the solution will be forced on the subspace of Φ_1 which is also what happens at the convergence of the original problem.

3.4 Effect of a baseline cut on the residuals

One strategy to avoid suppression of the desired 21-cm signal is to exclude the baselines on which we want to preserve the signal from the calibration data. Patil et al. (2017) follow such a strategy by removing all the baselines below 250λ from the calibration data. Although this indeed eliminates suppression on shorter baselines, it also causes an increased power, denoted by ‘excess noise’, on the residuals for the excluded baselines. In this section, we derive the expression for the residuals on the excluded baseline, and in the next section, we show, by simulations, how this strategy affects the power spectrum. While it is possible to include the baseline cut in the mask matrix, \mathbf{M} , the expression for the residual given in previous sections would then only be valid for the visibilities which are included during the calibration. We are mainly interested in the residuals on the removed baselines, and hence we reformulate this problem in a somewhat different way.

The calibration problem with a baseline cut can be formulated as

$$\hat{\theta} = \arg \min_{\theta} \|\mathbf{P}_{\text{sb}}^{\perp} [\hat{\mathbf{r}} - \mathbf{r}(\theta)]\|_2^2 + \sum_q \gamma_q \theta_q^H (\Phi_2 \Phi_2^H \otimes \mathbf{I}_{2P}) \theta_q$$

subject to $\mathbf{P}_{\Phi}^{\perp} \theta = \mathbf{0}$,

where $\mathbf{P}_{\text{sb}}^{\perp}$ is a projection matrix that removes the short baselines from the data and \mathbf{P}_{sb} is the projection matrix that only retains the short baselines. This optimization problem is a slightly modified version of the problem discussed in Section 3.3.2. Using the semilinearity, the residuals on the removed baselines are found to be

$$\mathbf{e}(\hat{\theta}) = \mathbf{P}_{\text{sb}} [\mathbf{I} - \mathbf{Z}_{\text{sb}}(\hat{\theta})] \hat{\mathbf{r}}, \quad (13)$$

where

$$\mathbf{Z}_{\text{sb}} = \mathbf{J} [\mathbf{P}_{\Phi} \mathbf{J}^H \mathbf{P}_{\text{sb}}^{\perp} \mathbf{P}_{\Phi} + 2\Gamma(\Phi_2 \Phi_2^H \otimes \mathbf{I}_{2PQ})]^{\dagger} \mathbf{J}^H \mathbf{P}_{\text{sb}}^{\perp},$$

and we have dropped dependency on θ here for better readability. The main difference between the expression for \mathbf{Z}_{sb} and \mathbf{Z} from the previous sections is the term $\mathbf{J}^H \mathbf{P}_{\text{sb}}^{\perp} \mathbf{J}$. Ignoring the regularization term for the moment, we see that this matrix indicates the level with which the gains can be calibrated independently of the removed baselines. If this term is singular, it indicates that the (unconstrained) problem is not identifiable and if it is badly conditioned, it will result in signal amplification. In the next section we see that this is exactly what happens, especially if the sky-model errors are large. In order to gain more insight into the suppression behaviour of gain calibration, we need to test these results with a sufficiently realistic model. That is the objective of the next section.

4 SIMULATIONS OF 21-CM SIGNAL SUPPRESSION

Given a realistic simulation of an instrument, we can directly calculate the suppression of any 21-cm signal during the calibration process, in the context of a calibration model that consists of multiple source clusters, an unmodelled component of the sky, and the desired 21-cm signal plus noise. In this section, we use LOFAR (van Haarlem et al. 2013) and the LOFAR EoR KSP calibration approach (see Patil et al. 2017, for details) as an example for testing the differences between various calibration approaches. We study the suppression using a Gaussian random field for the 21-cm signal which is maximally white (spatially and in frequency), on the chosen frequency range and below 250λ , in order to see the effect equally well on all scales of interest. Given that the signal suppression is scale dependent but relative, the exact choice of the 21-cm

signal is of secondary nature since it drops out when calculating the ratio between the input and output signal and only if chosen too strong might it affect the gain solutions.

4.1 Simulation set-up

For the following simulations we assume $P = 62$ receivers (i.e. LOFAR stations) and a model of the North Celestial Pole, which is one of the fields used for 21-cm EoR signal detection with LOFAR-HBA. We use the model that is currently used for calibration of the LOFAR-EoR data (Patil et al. 2017). We have simplified the model slightly by replacing some compact Gaussian sources with point sources of equal magnitude, which is not a relevant change. We use $K = 53$ sub-bands with a bandwidth of 195.3 kHz which gives us approximately a total bandwidth of 10 MHz centred symmetrically around 150 MHz. The $\sim 28\,000$ source components are split into $Q = 122$ clusters spread around the sky, but predominantly inside the primary beam of LOFAR-HBA. For simplicity, although this is motivated by the slow changes in gains in LOFAR, we assume the gains to remain constant (or coherent) during 10 min and the data to have a time resolution of 1 s which gives $T = 600$. Sampling at the Nyquist rate, we have $N = \lceil 2 \times 195.3 \times 10^3 \rceil$ electric field measurements for each snapshot of 1 s and each receiver. An additional noise term is added to account for the receiver noise and a constant sky temperature using \mathbf{R}_n . We simulate the 21-cm signal only on baselines with a length less than 250λ . These baselines are also used to make the final baseline-delay power spectra. On the longer baselines, the signal is too weak to be detected by LOFAR. The algorithm used is a Newton-based algorithm with a stopping criterion $\|\partial f(\boldsymbol{\theta})/\partial \boldsymbol{\theta}\| < 10^{-8}$ which is small enough for $\hat{\boldsymbol{\theta}}$ to be a critical point of the cost function and to ensure that the relations used for suppression are valid. The technical details of the algorithm are beyond the scope of this paper and will be reported separately. For the smooth basis functions, we use a polynomial set. The maximum allowed freedom for these polynomials is chosen to be three which means that $M = 4$. We chose the large-scale fluctuation of the gains for 10 MHz to be dominated by a first-order polynomial, which makes $M_1 = 2$.

4.2 Suppression tests using the complete sky model

4.2.1 Various scenarios

We test the 21-cm signal suppression in two scenarios. In one scenario we carry out a full smooth gain estimation (Scenario 1) and in the other scenario (Scenario 2) we study the effect of enforcing only Φ_1 , but terminating before convergence, as discussed in Section 3.3. This means that in Scenario 1, $M_1 = 2$, $M_2 = 2$ while in Scenario 2 we have $M_1 = 2$ and $M_2 = K - M_1$. We choose a much larger regularization term for the latter in order to emulate premature termination after several iterations. The sky model is used for both the generation of the data as well as calibration and hence except for the 21-cm signal and noise there are no addition signals, i.e. $\mathbf{r}_f = \mathbf{0}$. The matrix \mathbf{V} is constructed, and then, via an economical QR decomposition, Φ is obtained. The gains are generated as the sum of two components for each part of Φ . The expected values of the gains are generated with Φ_1 and a proper complex normal distributed random variables with a variance $\sigma^2 = 0.07$ is generated for Φ_2 . The regularization terms are then chosen uniformly with $\gamma_q = 1/\sigma^2$ for the full smooth calibration in Scenario 1. For the second simulation, Scenario 2, we use $\gamma_q = 100/\sigma^2$ to account for several iterations that forces the solutions closer to Φ_1 , but not exactly on the subspace

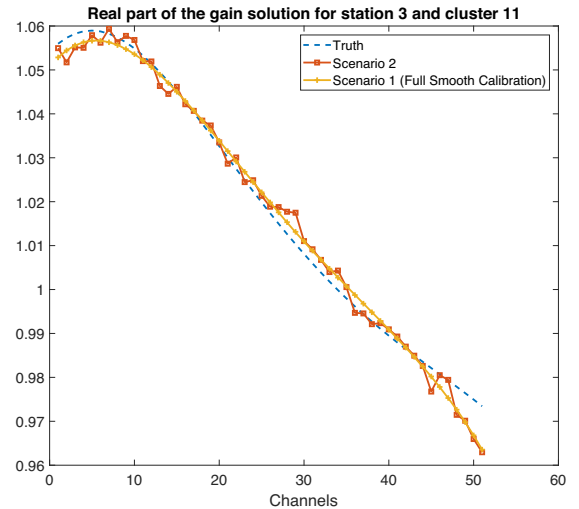


Figure 1. Real part of the gain solutions as a function frequency for a single station and cluster.

spanned by Φ_1 . This approach is similar to Scenario 1, but mimics terminating optimization before convergence, hence leaving extra gain fluctuations from Φ_2 in the solution.

4.2.2 Results and discussions

Fig. 1 illustrates an example of the difference between the solutions for the two scenarios. As expected the solution for Scenario 1 is much smoother and as a result has a much smaller degree of freedom (i.e. less dimensions are projected out). This is confirmed by the power-spectrum results illustrated in Fig. 2 (left-hand panel). The latter figure clearly shows that if smoothness is not exactly enforced, a large portion of the 21-cm signal power spectrum is heavily suppressed (up to an order of magnitude). It is important to note that if the suppression is expressed in the terms of the 2-norm of the signal $\|\mathbf{Z}\mathbf{r}_{21}\|_2/\|\mathbf{r}_{21}\|_2$ only a suppression of 17 per cent is estimated for Scenario 2. This indicates that calculating the power spectrum, in the region of interest, gives a much more accurate picture of suppression. Suppression is stronger on the shorter baselines and smaller delays. We note that this suppression on short baselines is similar to that seen by Patil et al. (2016). The polynomial basis function used is of order three, undulating on scales of $\sim 0.3\mu\text{s}$ or smaller. Any scale corresponding to a delay below this value can therefore be modelled away by this basis function, and it is exactly where the suppression increases rapidly.

4.3 Suppression test with an incomplete sky model

The final simulation is that where the sky model is incomplete, which is much closer to a realistic calibration scheme. The set-up for this simulation is similar to the one in the previous section with the exception that all the sources in the model which are smaller than 1 mJy are removed from the calibration model. This adds an additional foreground term and $\mathbf{r}_f \neq \mathbf{0}$. Again we calculate the power spectra for both scenarios and compute the suppression. Fig. 2 (bottom row) shows that using an incomplete sky model the suppression is more prominent even when we fully enforce smoothness. This effect can be explained using the results in Appendix C which show that the suppressed part of the 21-cm signal is proportional to the error in the model, $\mathbf{r}(\hat{\boldsymbol{\theta}}) - \mathbf{r}(\boldsymbol{\theta})$, and the foreground term \mathbf{r}_f , which

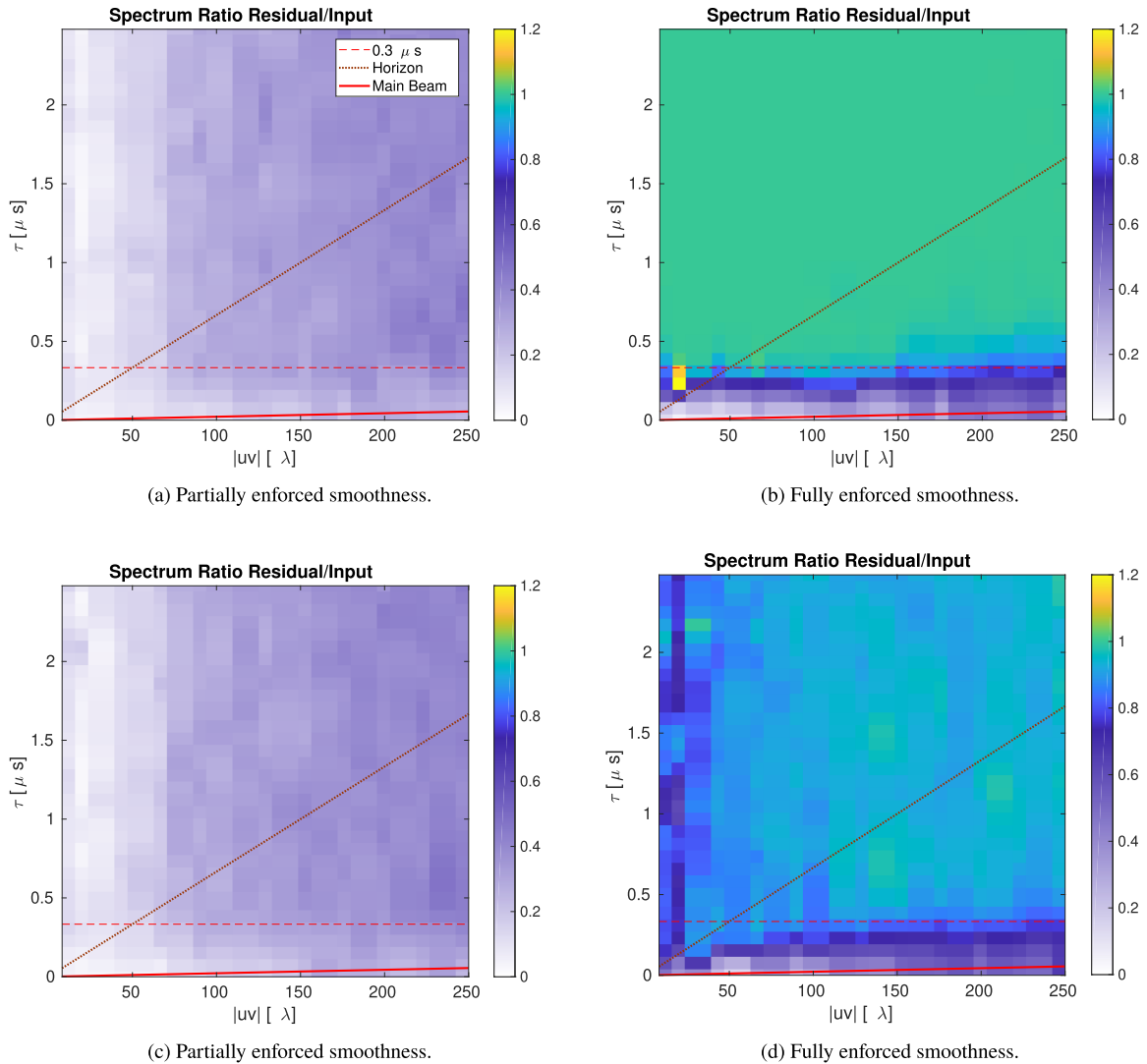


Figure 2. Top row: The ratio of the power spectra for the output and the input 21-cm signals. The left-hand panel shows their ratio when a complete sky model is used in the calibration, but allowing for some residual fluctuations of the gains around a smooth model, mimicking non-convergence or regularization. The right-hand panel shows the ratio when one forces the solutions to lie exactly on a smooth model of low order. The signal suppression at short delays are due to the allowed gain-model variations on several MHz scales. The scale where this suppression starts is generally set by the frequency-scale of the smoothness of the instrumental gains and then matched by the scale of the smoothness of gain model. In this simulation, this is assumed to be $\gtrsim 3$ MHz, corresponding to $\tau \lesssim 0.3 \mu\text{s}$. This indeed corresponds to where suppression of the signal is significant. Bottom row: idem, for an incomplete sky model.

are both larger in this scenario. Hence sky-incompleteness in the calibration model leads to enhanced 21-cm signal suppression. Although, to limit computational effort, we have removed sources < 1 mJy from the model, rather than adding sources below the lower flux limit present in it, to demonstrate the effect of model incompleteness visually. We note that in reality the removed sources are part of the LOFAR sky model and hence the level of suppression is likely to be smaller than illustrated in Fig. 2 (bottom row).

4.4 Suppression test with a baseline cut

In this section, we will repeat all four tests done, in the previous sections, with the additional modification of a baseline cut. All the baselines below 250λ are removed from the data before the calibration, similar to the approach by Patil et al. (2017), and

the effect of this operation on the power spectrum is studied. The results illustrated in Fig. 3 show the ratio of the spectra for both complete and incomplete sky models. By comparing these results with the results from previous sections, we see that the suppression behaviour of the algorithm in the case of partial smoothness is significantly improved. We note that this is the calibration strategy taken in Patil et al. (2017). We also see that where the signal was mainly suppressed, it is now amplified, which indicates degeneracy in the calibration model on those scales. This effect has also been seen by Patil et al. (2017) and earlier described by Trott & Wayth (2016). These figures also illustrate that both with and without a baseline cut it is beneficial to enforce smoothness more rigorously. Both the suppression and amplification of the signal (and with high probability also the leakage terms) are reduced, which agrees with the results found by Ewall-Wice et al. (2017).

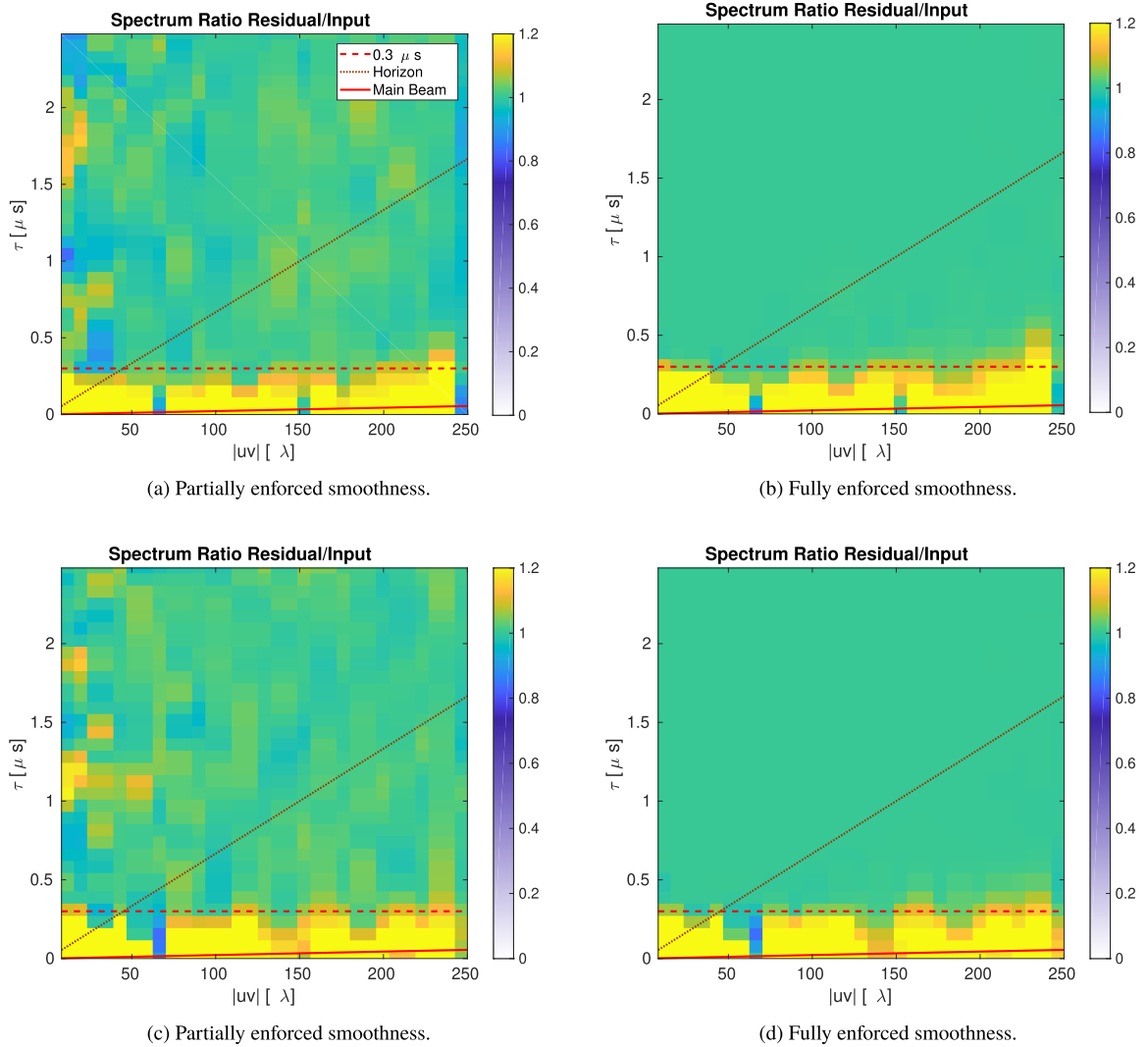


Figure 3. Top row: The same as in Fig. 2 excluding baselines at $<250\lambda$ during calibration. Bottom row: The same as in Fig. 2 for an incomplete sky model and excluding baselines at $<250\lambda$ during calibration.

5 CONCLUSIONS

In this paper, we have presented the first theoretical model that allows one to quantify the suppression of the cosmological 21-cm signal, due to direction-dependent gain calibration of radio-telescope receivers (e.g. dishes or aperture-arrays). By exploiting the ‘semilinearity’ property of the gain calibration models, we have shown that this suppression can be quantified with high precision and, as long as the signal is weak and does not bias the gain solutions themselves strongly, the result is independent of the 21-cm signal itself. The closed-form expressions for the residuals, that we present, allow one to study various leakage terms and clearly illustrate the trade-offs inherent to the calibration problem and the choices that are made (e.g. completeness of the sky model, number of directions to solve for, number of frequency channels to include, the level smoothness enforced on the solutions, baseline cut, etc.). We have found the following main results:

(1) If the sky model is complete, constraining and regularizing direction-dependent gain solutions to be smooth functions of frequency reduces suppression of the 21-cm signal to nearly zero on all short baselines, above a delay that corresponds roughly to the

scales on which the gains can vary. We demonstrate this for LO-FAR, showing that its current direction-dependent gain calibration (as described in Yatawatta 2016) in just over a hundred directions, is a feasible approach as long as the solutions are enforced to be smooth on scales larger than several MHz, and assuming that also the true gains are smooth on those scales (which is an instrument requirement for *any* successful 21-cm detection).

(2) To our knowledge, a novel result is that an incomplete sky model does not only cause leakage of strong foreground signals into the cosmological 21-cm signal as shown by Barry et al. (e.g. 2016) and Patil et al. (e.g. 2016), but it also degrades the quality of the 21-cm residuals and increases the level of signal suppression even if smoothness is fully enforced. This approach increases the 21-cm signal suppression even if the foregrounds and the 21-cm signals are entirely uncorrelated.

(3) Finally we find that introducing a baseline cut, where one calibrates the signal on shorter baselines using only the longer baselines, removes signal suppression, but conversely causes an enhanced signal when the sky model is incomplete. Enforcing spectral smoothness, however, as also shown by Ewall-Wice et al. (2017), removes this signal enhancement.

Although we conclude that forcing the gain solutions on smooth functions is an absolute requirement for 21-cm signal detection experiments [see discussions on these requirements in Barry et al. (2016), Trott & Wayth (2016), and Yatawatta (2016)], as is having a sky model that is as complete as possible, in practice this is computationally often very expensive. Performing for example 30–40 iterations of a full Newton-based calibration or increasing the number of sky-model components by an order of magnitude is not feasible when thousands of hours of data (petabytes) have to be processed. Both are crucial to avoid significant suppressing of the desired 21-cm signal. Adding a baseline cut mitigates suppression at the cost of enhancing power due to calibrating on an incomplete sky model. Finding the right balance between enforcing sufficient smoothness and reaching full convergence and having a sufficiently complete sky model, as attempted in the calibration approach of Yatawatta (2016), is therefore essential for detecting and properly quantifying the 21-cm signal.

A final conclusion is that our simulations for LOFAR strongly suggest that the low-frequency part of the Square Kilometre Array (i.e. SKA-low), being very similar to LOFAR in its layout and having a much improved instantaneous sensitivity and uv-coverage, should also be calibratable in at least ~ 100 directions for each station over a frequency band ~ 10 MHz and on time-scales less than 10 min. The underlying requirement for this to succeed, however, is that the direction-dependent receiver gains of the stations, as well as the model gains, should be intrinsically smooth on scales of at least several-MHz frequency scales, or larger, and that the gain-calibration sky model is complete to the mJy level. This conclusion is in line with the conclusions drawn by Trott & Wayth (2016).

ACKNOWLEDGEMENTS

AMS and LVEK acknowledge support from an SKA-NL Roadmap grant from the Dutch ministry of Education Culture and Science. We also thank Sarod Yatawatta for providing us with the LOFAR NCP sky model, and for very useful discussions and feedback. We also thank André Offringa, Florent Mertens, Bharat Gehlot, and Maaijke Mevius for useful discussions on gain calibration and modelling.

REFERENCES

- Asad K. M. B. et al., 2015, *MNRAS*, 451, 3709
 Barry N., Hazelton B., Sullivan I., Morales M. F., Pober J. C., 2016, *MNRAS*, 461, 3135
 Beardsley A. P. et al., 2013, *MNRAS*, 429, L5
 Boonstra A.-J., van der Veen A.-J., 2003, *IEEE Tran. Signal Process.*, 51, 25
 Craven P., Wahba G., 1978, *Numer. Math.*, 31, 377
 DeBoer D. R. et al., 2017, *PASP*, 129, 045001
 Di Matteo T., Perna R., Abel T., Rees M. J., 2002, *ApJ*, 564, 576
 Ewall-Wice A., Dillon J. S., Liu A., Hewitt J., 2017, *MNRAS*, 470, 1849
 Furlanetto S. R., Oh S. P., Briggs F. H., 2006a, *Phys. Rep.*, 433, 181
 Furlanetto S. R., Peng Oh S., Briggs F. H., 2006b, *Phys. Rep.*, 433, 181
 Grobler T. L., Nunhokee C. D., Smirnov O. M., van Zyl A. J., de Bruyn A. G., 2014, *MNRAS*, 439, 4030
 Grobler T. L., Stewart A. J., Wijnholds S. J., Kenyon J. S., Smirnov O. M., 2016, *MNRAS*, 461, 2975
 Harker G. et al., 2010, *MNRAS*, 405, 2492
 Jelić V. et al., 2008, *MNRAS*, 389, 1319
 Kazemi S., Yatawatta S., Zaroubi S., 2013, *MNRAS*, 434, 3130
 Koopmans L. et al., 2015, in Proceedings of Advancing Astrophysics with the Square Kilometre Array (AASKA14), Giardini Naxos, Italy. p. 1

- McQuinn M., Zahn O., Zaldarriaga M., Hernquist L., Furlanetto S. R., 2006, *ApJ*, 653, 815
 Mertens F., Ghosh A., Koopmans L., 2018, *MNRAS*, 478, 3640
 Morales M. F., Wyithe J. S. B., 2010, *ARA&A*, 48, 127
 Mouri Sardarabadi A., 2016, PhD thesis, Delft Univ. Technology
 Mouri Sardarabadi A., van der Veen A.-J., 2014, in 2014 IEEE 8th Sensor Array and Multichannel Signal Processing Workshop (SAM), IEEE, A Coruna, Spain, p. 153
 Offringa A. R., van de Gronde J. J., Roerdink J. B. T. M., 2012, *A&A*, 539, A95
 Offringa A. R. et al., 2013, *A&A*, 549, A11
 Offringa A. R. et al., 2015, *PASA*, 32, 54
 Oh S. P., Mack K. J., 2003, *MNRAS*, 346, 871
 Parsons A., Pober J., McQuinn M., Jacobs D., Aguirre J., 2012, *ApJ*, 753, 81
 Patil A. et al., 2017, *ApJ*, 838, 65
 Patil A. H. et al., 2016, *MNRAS*, 463, 4317
 Pritchard J. R., Loeb A., 2012, *Rep. Prog. Phys.*, 75, 6901
 Rohde C. A., 1965, *J. Soc. Ind. Appl. Math.*, 13, 1033
 Schreier P. J., 2010, *Statistical Signal Processing of Complex-Valued Data*. Cambridge Univ. Press, Cambridge
 Smirnov O., Tasse C., 2015, *MNRAS*, 449, 2668
 Sokolowski M., Wayth R. B., Lewis M., 2015, 2015 IEEE Global Electromagnetic Compatibility Conference (GEMCCON), IEEE, Adelaide, Australia, p. 1
 Trott C. M., Wayth R. B., 2016, *PASA*, 33, e019
 van Haarlem M. P., Wise M. W., Gunst A. W. et al., 2013, *A&A*, 556, A2
 van der Tol S., Jeffs B., van der Veen A.-J., 2007, *IEEE Trans. Signal Process.*, 55, 4497
 Wijnholds S., van der Veen A.-J., 2009, *IEEE Trans. Signal Process.*, 57, 3512
 Wijnholds S. J., Grobler T. L., Smirnov O., 2016, *MNRAS*, 457, 2331
 Yatawatta S., 2015, *MNRAS*, 449, 4506
 Yatawatta S., 2016, 2016 24th European Signal Processing Conference (EUSIPCO), IEEE, Budapest, Hungary, p. 265

APPENDIX A: SEMILINEARITY OF DDC

In this section, we illustrate that the model used in Section 2 satisfies the semilinearity property. We define a general form of semilinear functions and some of their properties. We call any vector-valued vector-function $\mathbf{f}(\boldsymbol{\theta})$ (i.e. a mapping from $\mathbb{C}^m \rightarrow \mathbb{C}^n$) for which holds

$$\mathbf{f}(\boldsymbol{\theta}) = \mathbf{J}\mathbf{C}\boldsymbol{\theta}, \quad (\text{A1})$$

where $\mathbf{J} = \partial\mathbf{f}(\boldsymbol{\theta})/\partial\boldsymbol{\theta}^T$ is the Jacobian matrix of $\mathbf{f}(\boldsymbol{\theta})$ and \mathbf{C} is a constant matrix, semilinear.

The following properties hold for functions with semilinear property:

(i) If two semilinear functions $\mathbf{f}_1(\boldsymbol{\theta})$ and $\mathbf{f}_2(\boldsymbol{\theta})$ share the same constant matrix \mathbf{C} , then the function obtained by stacking them is also semilinear with the same \mathbf{C} , i.e.

$$\mathbf{f}_3(\boldsymbol{\theta}) = \begin{bmatrix} \mathbf{f}_1(\boldsymbol{\theta}) \\ \mathbf{f}_2(\boldsymbol{\theta}) \end{bmatrix} = \begin{bmatrix} \mathbf{J}_1 \\ \mathbf{J}_2 \end{bmatrix} \mathbf{C}\boldsymbol{\theta},$$

where $\mathbf{J}_i = \partial\mathbf{f}_i(\boldsymbol{\theta})/\partial\boldsymbol{\theta}^T$ for $i = 1, 2$.

(ii) A linear transformation of the form $\boldsymbol{\theta} = \mathbf{B}\boldsymbol{\theta}_1$ keeps the semilinearity property with new constant matrix that satisfies

$$\mathbf{B}\mathbf{C}_1 = \mathbf{C}\mathbf{B},$$

i.e. $\mathbf{f}(\mathbf{B}\boldsymbol{\theta}_1) = \mathbf{J}_1\mathbf{C}_1\boldsymbol{\theta}_1$, where $\mathbf{J}_1 = \partial\mathbf{f}(\boldsymbol{\theta}_1)/\partial\boldsymbol{\theta}_1^T$.

(iii) For the sum of two semilinear functions with different variables, e.g. $\mathbf{f}_1(\theta_1)$ and $\mathbf{f}_2(\theta_2)$ where $\partial\theta_1/\partial\theta_2^T = \mathbf{0}$, we have

$$\begin{aligned}\mathbf{f}_3(\theta_1, \theta_2) &= \mathbf{f}_1(\theta_1) + \mathbf{f}_2(\theta_2) \\ &= [\mathbf{J}_1 \quad \mathbf{J}_2] \begin{bmatrix} \mathbf{C}_1 & \mathbf{0} \\ \mathbf{0} & \mathbf{C}_2 \end{bmatrix} \begin{bmatrix} \theta_1 \\ \theta_2 \end{bmatrix},\end{aligned}$$

and hence, $\mathbf{f}_3(\theta_1, \theta_2)$ is also semilinear.

Because the vector $\mathbf{r}(\theta)$ is formed by stacking the covariance matrices for a single snapshot at a single frequency channel, we can show the semilinearity for a single snapshot first, and then use property (i) to show this for $\mathbf{r}(\theta)$. We can also use property (iii) to generalize a model with a single cluster, to a model with multiple clusters. Therefore using these two properties, we only need to show that semilinearity holds for $Q = 1$ (e.g. direction-independent gain calibration). The model for a single snapshot and cluster is given by

$$\mathbf{R} = \mathbf{M} \odot \mathbf{G} \boldsymbol{\Sigma} \mathbf{G}^H = \mathbf{G}(\mathbf{M} \odot \boldsymbol{\Sigma}) \mathbf{G}^H,$$

where \odot is the element-wise multiplication of two matrices of the same size. Hence, without loss of generality, we can take the flagging into the sky model as $\tilde{\boldsymbol{\Sigma}} \equiv \mathbf{M} \odot \boldsymbol{\Sigma}$ and rewrite the vectorized measurement equation as

$$\mathbf{r} = \text{vect}(\mathbf{R}) = (\mathbf{G}^* \tilde{\boldsymbol{\Sigma}}^T \circ \mathbf{I}_P) \mathbf{g} = (\mathbf{I}_P \circ \mathbf{G} \tilde{\boldsymbol{\Sigma}}) \mathbf{g}^*, \quad (\text{A2})$$

where $\mathbf{g} = \text{vectdiag}(\mathbf{G})$ is the $P \times 1$ vector of complex gains and we used the property $\text{vect}(\mathbf{A}\mathbf{B}\mathbf{B}) = (\mathbf{B}^T \circ \mathbf{A})\text{vectdiag}(\mathbf{B})$ with \circ as the Khatri-Rao (or column-wise Kronecker) product and \mathbf{D} a diagonal matrix. Using these two presentations for $\theta = [\mathbf{g}^T, \mathbf{g}^H]^T$ we have

$$\mathbf{J} = \frac{\partial \mathbf{r}(\theta)}{\partial \theta^T} = [\mathbf{G}^* \tilde{\boldsymbol{\Sigma}}^T \circ \mathbf{I}_P, \mathbf{I}_P \circ \mathbf{G} \tilde{\boldsymbol{\Sigma}}].$$

To show the semilinearity of $\mathbf{r}(\theta)$ we need to show that equation (8) holds. In order to do this we calculate

$$\begin{aligned}\mathbf{J}\theta &= [\mathbf{G}^* \tilde{\boldsymbol{\Sigma}}^T \circ \mathbf{I}_P, \mathbf{I}_P \circ \mathbf{G} \tilde{\boldsymbol{\Sigma}}] \begin{bmatrix} \mathbf{g} \\ \mathbf{g}^* \end{bmatrix} \\ &= (\mathbf{G}^* \tilde{\boldsymbol{\Sigma}}^T \circ \mathbf{I}_P) \mathbf{g} + (\mathbf{I}_P \circ \mathbf{G} \tilde{\boldsymbol{\Sigma}}) \mathbf{g}^* = 2\mathbf{r},\end{aligned}$$

which as expected leads to $\mathbf{C} = 1/2\mathbf{I}_{2*P}$. We see that \mathbf{C} does not depend on frequency, time, or direction. Now we can use property (iii) to generalize these results to cases where $Q > 0$ which leads to $\mathbf{C} = 1/2\mathbf{I}_{2QP}$. Similarly for a smooth basis we should note that Φ is a unitary matrix and hence $\Phi^\dagger = \Phi^H$ and using property (ii) with $\mathbf{B} = \Phi \otimes \mathbf{I}$ we get

$$\mathbf{C} = \frac{1}{2}(\Phi \otimes \mathbf{I})^\dagger (\Phi \otimes \mathbf{I}) = \frac{1}{2}\mathbf{I}_{2QPM}.$$

Except for the dimensions, the constant matrix \mathbf{C} is the same for all the transformations of DDC we have applied throughout this manuscript.

APPENDIX B: BAYSIAN INFERENCES AND SEMILINEARITY

In this section, we use the maximum a posteriori estimator (MAP) to both show a detailed derivation of the matrix \mathbf{Z} and its statistical interpretation. We start by the definition of the MAP estimator, which is given by

$$\hat{\theta}_{\text{MAP}} = \arg \max_{\theta} p(\mathbf{Y}|\theta)p(\theta),$$

where $p(\mathbf{Y}|\theta)$ is the probability distribution function (PDF) of the observed voltages given the gains (with \mathbf{Y} a $KTP \times N$ data matrix

of all measured voltages) and $p(\theta)$ is the prior PDF for the gains. Another way to achieve the same results is using the log-likelihood instead of the PDF. In this case the MAP estimator can be written as

$$\hat{\theta}_{\text{MAP}} = \arg \min_{\theta} l(\mathbf{Y}|\theta) + l(\theta), \quad (\text{B1})$$

where $l(\mathbf{Y}|\theta) = -\ln(p(\mathbf{Y}|\theta))$ and $l(\theta) = -\ln(p(\theta))$. We already know that \mathbf{Y} is a proper complex Gaussian random variable with zero mean and its covariance matrix is given by the matrices $\mathbf{R}_{t,k}$. For θ we also assume a proper complex Gaussian random variable with $\mathcal{E}\{\theta\} = (\Phi_1 \otimes \mathbf{I}_{2PQ})\alpha_1$ and covariance $\mathbf{C}_\theta = \Gamma^{-1}(\Phi_2 \Phi_2^H \otimes \mathbf{I}_{2PQ})$. Using these distributions, at the solution we have

$$\frac{\partial [l(\mathbf{Y}|\theta) + l(\theta)]}{\partial \theta^T} = \mathbf{P}_\Phi \mathbf{J}^H [\mathbf{C}_\epsilon(\theta)]^{-1} (\mathbf{r}(\theta) - \hat{\mathbf{r}}) + \mathbf{C}_\theta^\dagger \theta = \mathbf{0}, \quad (\text{B2})$$

where $\mathbf{J} = \partial \mathbf{r}(\theta)/\partial \theta^T$ and

$$\mathbf{C}_\epsilon(\theta) = \begin{bmatrix} \mathbf{R}_{1,1}^T \otimes \mathbf{R}_{1,1} & & & \\ & \ddots & & \\ & & \ddots & \\ & & & \mathbf{R}_{T,K}^T \otimes \mathbf{R}_{T,K} \end{bmatrix},$$

with

$$\mathbf{R}_{t,k} = \sum_q \mathbf{G}_{q,t,k} \boldsymbol{\Sigma}_{q,t,k} \mathbf{G}_{q,t,k}^H + \mathbf{R}_{n,t,k}.$$

Now using the semilinearity property and (B2) we have

$$\mathbf{P}_\Phi \left(\frac{1}{2} \mathbf{J}^H [\mathbf{C}_\epsilon(\theta)]^{-1} \mathbf{J} + \mathbf{C}_\theta^\dagger \right) \mathbf{P}_\Phi \theta = \mathbf{P}_\Phi \mathbf{J}^H [\mathbf{C}_\epsilon(\theta)]^{-1} \hat{\mathbf{r}},$$

where we used the fact that $\mathbf{C}_\theta^\dagger = \mathbf{P}_\Phi \mathbf{C}_\theta^\dagger \mathbf{P}_\Phi$. This system of equations is consistent and hence we find the solution

$$\theta = 2 \left[\mathbf{P}_\Phi (\mathbf{J}^H [\mathbf{C}_\epsilon(\theta)]^{-1} \mathbf{J} + 2\mathbf{C}_\theta^\dagger) \mathbf{P}_\Phi \right]^\dagger \mathbf{P}_\Phi \mathbf{J}^H [\mathbf{C}_\epsilon(\theta)]^{-1} \hat{\mathbf{r}}$$

and the residuals become

$$\mathbf{e}(\theta) = \hat{\mathbf{r}} - \mathbf{J} \mathbf{P}_\Phi \left[\mathbf{P}_\Phi (\mathbf{J}^H [\mathbf{C}_\epsilon(\theta)]^{-1} \mathbf{J} + 2\mathbf{C}_\theta^\dagger) \mathbf{P}_\Phi \right]^\dagger \mathbf{P}_\Phi \mathbf{J}^H [\mathbf{C}_\epsilon(\theta)]^{-1} \hat{\mathbf{r}}.$$

To simplify these results to the regularized LS problem in Section 3.3.2 we need to replace \mathbf{C}_ϵ with the identity matrix. In this case the residuals become

$$\begin{aligned}\mathbf{e}(\theta) &= \hat{\mathbf{r}} - \mathbf{J} \left[\mathbf{P}_\Phi \mathbf{J}^H \mathbf{J} \mathbf{P}_\Phi + 2\Gamma(\Phi_2 \Phi_2^H \otimes \mathbf{I}_{2PQ}) \right]^\dagger \mathbf{J}^H \hat{\mathbf{r}} \\ &= [\mathbf{I} - \mathbf{Z}] \hat{\mathbf{r}},\end{aligned}$$

where we have removed some redundant projection matrices. Another way to reach the same expression is to use the Lagrange function of the regularized problem and use the semilinearity property. Using either a Bayesian methodology or the Lagrange function, the expression for \mathbf{Z}_{sb} can also be found in similar manner.

APPENDIX C: INCOMPLETENESS AND SUPPRESSION

The semilinearity allows us to write the relation between the residuals at any two points θ_1 and θ_2 as

$$\mathbf{e}(\theta_2) = \mathbf{e}(\theta_1) - \mathbf{r}(\Delta\theta) - \mathbf{J}(\theta_1)\Delta\theta,$$

where $\Delta\theta = \theta_2 - \theta_1$.

Two important points are the true gains, $\tilde{\theta}$ and the solution to the optimization problem $\hat{\theta}$. Using these two points in the relation above, we can express the removed part of the 21-cm signal as a

function of other contributors to the visibilities. For the residual at the solution we have

$$\mathbf{e}(\hat{\theta}) = \mathbf{e}(\tilde{\theta}) - \mathbf{r}(\Delta\theta) - \mathbf{J}(\tilde{\theta})\Delta\theta.$$

While this expression shows how the residual is related to the error in the solutions, $\hat{\theta} - \tilde{\theta}$, it does not show how exactly the error in the visibility affects these solutions. We know from equation (9) that at the solution $\mathbf{P}(\hat{\theta})\mathbf{e}(\hat{\theta}) = \mathbf{0}$. By multiplying both sides of the expression above by $\mathbf{P}(\hat{\theta})$ and writing out the expression for $\mathbf{e}(\tilde{\theta})$ we have

$$\mathbf{P}(\hat{\theta}) \left[\mathbf{r}(\tilde{\theta}) - \mathbf{r}(\hat{\theta}) - \mathbf{r}_{21}(\tilde{\theta}) - \mathbf{r}_f(\tilde{\theta}) - \epsilon \right] = \mathbf{0}$$

or

$$\mathbf{P}(\hat{\theta})\mathbf{r}_{21}(\tilde{\theta}) = \mathbf{P}(\hat{\theta}) \left[\mathbf{r}(\tilde{\theta}) - \mathbf{r}(\hat{\theta}) - \mathbf{r}_f(\tilde{\theta}) - \epsilon \right]. \quad (\text{C1})$$

This shows that the suppressed part of the 21-cm signal is proportional to the error in the model, $\mathbf{r}(\tilde{\theta}) - \mathbf{r}(\hat{\theta})$, which is the result of noisy/biased solutions and foregrounds. This also shows that when \mathbf{r}_f is large, it contributes two times to the signal degradation. The first contribution is direct and the second is by increasing the bias in $\hat{\theta}$ and hence increasing $\mathbf{r}(\tilde{\theta}) - \mathbf{r}(\hat{\theta})$.

This paper has been typeset from a $\text{\TeX}/\text{\LaTeX}$ file prepared by the author.